ACS APPLIED MATERIALS & INTERFACES

Research Article

www.acsami.org

Facile and Scalable Synthesis of $Zn_3V_2O_7(OH)_2{\cdot}2H_2O$ Microflowers as a High-Performance Anode for Lithium-Ion Batteries

Haowu Yan,[†] Yanzhu Luo,[*,†,‡] Xu Xu,[†] Liang He,[†,§] Jian Tan,[†] Zhaohuai Li,[†] Xufeng Hong,[†] Pan He,[†] and Liqiang Mai[*,†,∥]

[†]State Key Laboratory of Advanced Technology for Materials Synthesis and Processing, Wuhan University of Technology, Wuhan 430070, People's Republic of China

[‡]College of Science, Huazhong Agricultural University, Wuhan 430070, People's Republic of China

[§]Department of Materials Science and NanoEngineering, Rice University, Houston, Texas 77005, United States

[∥]Department of Chemistry, University of California, Berkeley, California 94720, United States

Supporting Information

ABSTRACT: The employment of nanomaterials and nanotechnologies has been widely acknowledged as an effective strategy to enhance the electrochemical performance of lithium-ion batteries (LIBs). However, how to produce nanomaterials effectively on a large scale remains a challenge. Here, the highly crystallized $Zn_3V_2O_7(OH)_2{\cdot}2H_2O$ is synthesized through a simple liquid phase method at room temperature in a large scale, which is easily realized in industry. Through suppressing the reaction dynamics with ethylene glycol, a uniform morphology of microflowers is obtained. Owing to the multiple reaction mechanisms (insertion, conversion, and alloying) during Li insertion/extraction, the prepared electrode delivers a remarkable specific capacity of 1287 mA h g^{-1} at 0.2 A g^{-1} after 120 cycles. In addition, a high capacity of 298 mA h g^{-1} can be obtained at 5 A g^{-1} after 1400 cycles. The excellent electrochemical performance can be attributed to the high crystallinity and large specific surface area of active materials. The smaller particles after cycling could facilitate the lithium-ion transport and provide more reaction sites. The facile and scalable synthesis process and excellent electrochemical performance make this material a highly promising anode for the commercial LIBs.

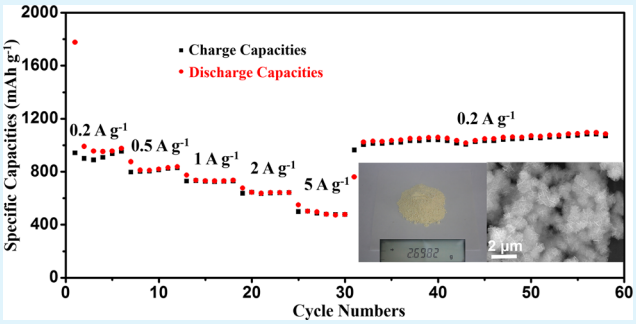

KEYWORDS: *$Zn_3V_2O_7(OH)_2{\cdot}2H_2O$, liquid phase method, Ostwald ripening, lithium-ion batteries, anode materials*

1. INTRODUCTION

With the exploding demand for LIBs with high energy density, it has become an essential and urgent task to extensively explore the alternative anode materials with higher theoretical capacity and ideal microstructure for next-generation LIBs.[1−4] Recently, transitional metal oxides as anodes for LIBs have attracted increasing attention due to their earth abundance, low cost, and high theoretical specific capacities (>600 mA h g^{-1}).[5−9] Ternary transitional metal oxides have demonstrated better cyclic performance, owing to the interfacial and synergistic effects between the two metallic elements.[10−12]

Since the first research on the vanadates as LIBs anodes by Tarascon's group in 1999,[13] ternary metal vanadates seem to become an important candidate as LIBs anode. Their intriguing electrochemical activities would be mainly benefiting from the multiple valence states of the vanadium element and layered structure for lithium-ion insertion/deinsertion.[14] As a result, numerous ternary metal vanadates have been extensively reported, including cobalt vanadates,[15−19] iron vanadates,[20,21] zinc vanadates,[22,23] etc. Ternary metal vanadates undergo multiple lithium reaction mechanisms during their electrochemical reaction: Li intercalation−deintercalation reaction with vanadium oxide, conversion reaction, or alloying−dealloying reaction, resulting in high specific capacities.[24−26] Despite their distinguished advantages, vanadates also suffer from the inherent poor electrical conductivity and repetitively large volume expansion/contraction upon cycling, leading to limited rate performance and poor capacity stability.[27−30]

To alleviate these issues, one effective strategy is to optimize the electrode materials to well-designed nanostructures with easy accessibility of lithium ions, short ion diffusion pathway, and abundant active sites for electrochemical reaction.[31−35] Two-dimensional (2D) nanosheets have been demonstrated to exhibit unique physical and chemical properties due to their atomic scale thickness, which can easily accommodate structure and volume change during electrochemical reaction.[36−38] However, the general strategy for synthesizing nanosheets materials is usually under strict experimental conditions (such

Received: May 17, 2017
Accepted: July 27, 2017
Published: July 27, 2017

DOI: 10.1021/acsami.7b06996
ACS Appl. Mater. Interfaces 2017, 9, 27707−27714

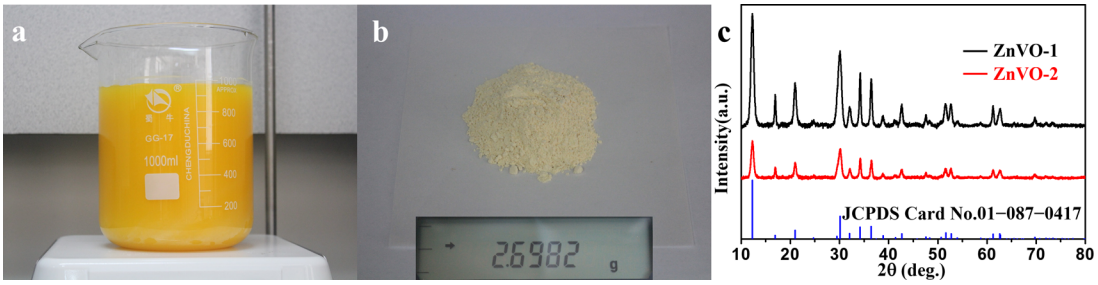

Figure 1. (a) Digital photo of the large-scale synthesis solution. (b) The digital photo of obtained powder and mass. (c) XRD patterns of ZnVO-1 and ZnVO-2.

as hydrothermal,[39] CVD-grown,[40] microwave routes,[41] etc.), with disadvantages of complicated synthesis steps and high cost for scalable synthesis.[42] On the basis of this issue, it is necessary to develop a simple and cost-effective strategy for the large-scale synthesis of nanosheets materials.

Here, we report a simple liquid phase precipitation method to synthesize $Zn_3V_2O_7(OH)_2{\cdot}2H_2O$ nanosheet-assembled microflowers at room temperature. In this hierarchical nanostructure, the ultrathin $Zn_3V_2O_7(OH)_2{\cdot}2H_2O$ nanosheets can provide abundant active sites and short pathways for Li ions, and the stress caused by volume expansion/extraction during the electrochemical processes can be well accommodated. Furthermore, the robust framework of the microflowers can effectively buffer the aggregation of nanosheets, leading to increased reversible capacity. Benefiting from this unique structure, the hierarchical $Zn_3V_2O_7(OH)_2{\cdot}2H_2O$ nanosheet-assembled microflowers exhibit a high specific capacity (1287 mA h g^{-1} at 0.2 A g^{-1}), excellent rate capability (501 mA h g^{-1} at 5 A g^{-1}), and long cycling life (298 mA h g^{-1} after 1400 cycles at 5 A g^{-1}).

2. EXPERIMENTAL SECTION

2.1. Materials Synthesis. In a typical process, $Zn_3V_2O_7(OH)_2{\cdot}2H_2O$ nanosheet-assembled microflowers were synthesized by a simple liquid phase precipitation procedure at room temperature without template assistance. A 10.536 g portion of $Zn(Ac)_2{\cdot}2H_2O$ was dissolved in 480 mL of deionized water to form a homogeneous solution, denoted as solution A. A 3.744 g portion of NH_4VO_3 was added to 320 mL of deionized water under stirring for 15 min at 80 °C, denoted as solution B. After that, the obtained solution B was added into solution A slowly and stirred for 10 min to form a yellow suspension. Then, 160 mL of ethylene glycol (EG) was added to the mixed solution and stirred for another 2 h to obtain the yellow precipitates. The precipitates were collected by centrifugation and washed with deionized water for 3 times. Then, the final product was obtained after freeze-drying for 72 h, which was marked as ZnVO-1. As the control experiment, ZnVO-2 was prepared using the same procedure without the addition of EG.

2.2. Characterization. The phase components and structure information on ZnVO-1 and ZnVO-2 were confirmed by X-ray powder diffraction (XRD, Bruker D8 Advance) equipped with a non-monochromated Cu Kα X-ray source. The microstructure and chemical components of ZnVO-1 and ZnVO-2 were characterized by field emission scanning electron microscope (FESEM, JEOL JSM-7100F) and high-resolution transmission electron microscope (HRTEM, JEOL JEM-2100F, 200 kV). The specific surface area and Barrett−Joyner−Halenda (BJH) pore size distribution were analyzed using a Micromeritics Tristar 3020 instrument. X-ray photoelectron spectroscopy analysis was conducted on a Thermo Scientific Escalab 250Xi.

2.3. Electrochemical Measurements. A homogeneous slurry was formed by mixing 70 wt % active materials, 20 wt % carbon black, and 10 wt % sodium alginate (SA) in a mortar and then was coated on copper foil to make the working electrode. The electrochemical performance was evaluated using a standard CR2016-type coin cell with copper foil as the current collector, lithium foil as reference electrode, polypropylene microporous films (Celgard 2400) as separator, and a 1 M solution of $LiPF_6$ in ethylene carbon (EC)/dimethyl carbonate (DMC) as electrolyte. These batteries were assembled in an Ar-filled glovebox with H_2O and O_2 contents less than 0.1 ppm. All electrochemical measurements were conducted at room temperature, and capacity values were calculated based on the weight of active materials. The active material masses per unit area of all prepared electrodes range from 0.86 to 1.12 mg cm^{-2}. The galvanostatic charge/discharge cycling performance of the active material in the voltage range of 0.01−3 V was evaluated by a LAND CT2001A multichannel battery testing system. Cyclic voltammetry (CV) measurements were performed by a CHI 660D electrochemical workstation in the cutoff voltage window of 0.01−3.0 V at a scan rate of 0.1 mV s^{-1}. Electrochemical impedance spectroscopy (EIS) was carried out by an Autolab PGSTAT 302N at the cell voltage of 2.1 V with a frequency range from 100 kHz to 0.01 Hz at a fixed perturbation amplitude of 10 mV.

3. RESULTS AND DISCUSSION

It is well-known that the mass of a prepared sample in the laboratory is usually as low as the milligram level, which is just sufficient for research purposes. Furthermore, most of the synthesis procedures involved high temperature treatment and/or high pressure environment, and demand a long time range. Though the excellent performance has been achieved, most of the exciting results are limited in the laboratory and difficult or even impossible to be scaled up economically. Herein, we performed a large-scale synthesis of hydrated zinc vanadate in the laboratory to illustrate the application potential of the as-described synthetic method. Over 2.6 g of final product can be easily obtained. The photographs of the reaction solution and final product are shown in Figure 1a,b. Ethylene glycol (EG) is employed in the reaction process to control the growth of the zinc vanadate. X-ray diffraction (XRD) patterns of the samples with (ZnVO-1) and without (ZnVO-2) EG in the reaction process can be both well-indexed to $Zn_3V_2O_7(OH)_2{\cdot}2H_2O$ in Figure 1c (JCPDS Card No. 01-087-0417), which has a layered structure composed of zinc oxide/hydroxide octahedral, with water molecules between the layers (Figure S1).[43] According to the previous literatures, the crystal water can work as a charge shielding layer of metal ions, maintain the layered crystal structure, and allow the effective diffusion of ions, thus leading to improved electrochemical activity of the electrode material.[44] Ethylene glycol (EG) is the key factor for the formation of products with high crystallinity and uniform morphology. Although ZnVO-1 and ZnVO-2 have the same diffraction peaks, ZnVO-2 exhibits lower peak intensity, indicating its lower crystallinity compared to ZnVO-1.

DOI: 10.1021/acsami.7b06996
ACS Appl. Mater. Interfaces 2017, 9, 27707−27714

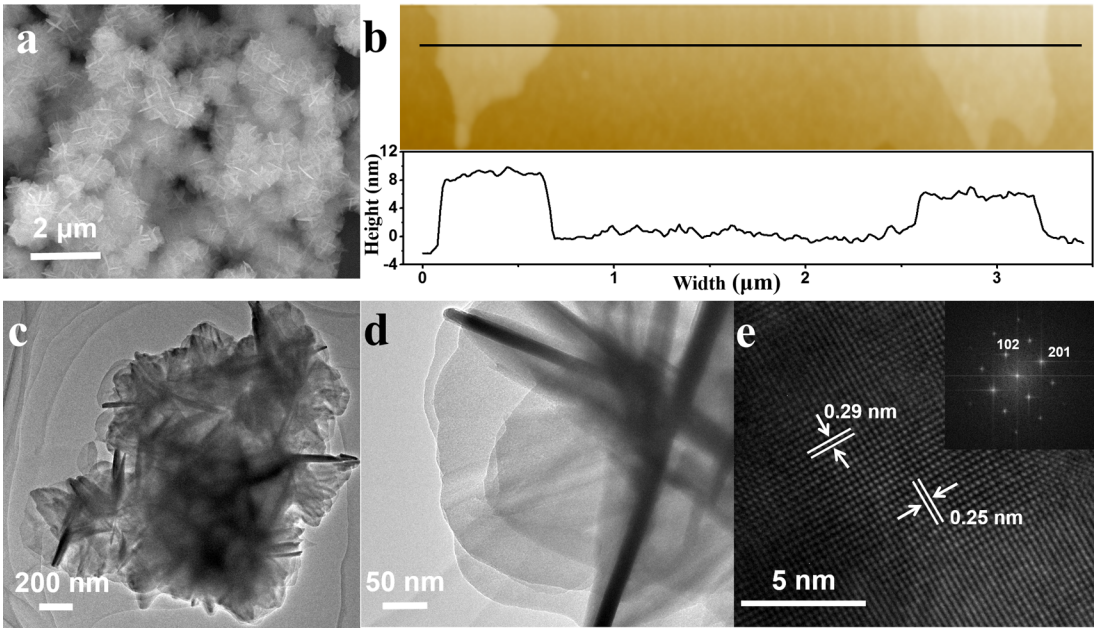

Figure 2. (a) SEM image of ZnVO-1. (b) AFM image of the ZnVO-1 nanosheets and the "height−width" profile. (c−e) TEM, HRTEM images, and FFT pattern of ZnVO-1.

The microstructures and surface morphologies of ZnVO-1 and ZnVO-2 were characterized by field-emission scanning electron microscopy (FESEM). The results in Figure 2a and Figure S2a obviously reveal that both of the materials display a uniform nanosheet-assembled microflowers structure. Detailed structural features of ZnVO-1 and ZnVO-2 were further characterized by high-resolution transmission electron microscopy (HRTEM) and atomic force microscopy (AFM). As shown in Figure 2b,d, the ZnVO-1 is composed of relatively uniform nanosheets with an average thickness of around 8 nm and a lateral size of 300−500 nm. Moreover, the clear lattice fringes with interplanar spacings of ca. 0.29 and 0.25 nm can be clearly observed, corresponding to the (102) and (201) crystal planes of hexagonal $Zn_3V_2O_7(OH)_2{\cdot}2H_2O$, respectively, indicating the single crystalline in nature. However, compared with ZnVO-1, ZnVO-2 is composed by more irregular nanosheets with a rough surface (Figure S2c,d). Furthermore, there is no long-range-ordering in ZnVO-2 nanocrystals, while a disordered state, which is confirmed by the fast Fourier transformation (FFT) pattern (Figure S2e). As shown in Figure S3, both of the isotherms of ZnVO-1 and ZnVO-2 can be classified as type IV with a distinct H3-type hysteresis loop.[45] The specific surface areas of ZnVO-1 and ZnVO-2 are 43.8 and 43.5 $m^2\ g^{-1}$, respectively. The N_2 adsorption/desorption isotherms possess relative pressure ranges of 0.51−1.0 for ZnVO-1 and 0.61−1.0 for ZnVO-2, respectively, which indicates the existence of a large number of mesopores and macropores. The higher relative pressure observed for the ZnVO-2 reveals more porosity and larger pore size than ZnVO-1.[46]

According to the previous reports, the structure evolution of nanosheet-assembled microflowers is proposed as follows.[47] During the synthesis process, a large number of tiny crystalline nuclei formed with the reaction between VO_3^- and Zn^{2+} ions. $Zn_3V_2O_7(OH)_2{\cdot}2H_2O$ has a layered crystal structure, which determines the anisotropic growth of crystal growth, leading to the formation of nanosheets.[48] In the next stage, the nanosheets would self-assemble into microflowers driven by the minimization of the system surface energy and experience further crystallization. However, with the existence of EG, the synthesis process would be different. EG has been widely employed as a cross-linking reagent to form metal glycolate with transition metal ions.[49] As the chainlike of zinc vanadium glycolate oligomers become sufficiently long, they could further self-assemble into uniform nanosheets, which would be larger than that of ZnVO-2. Furthermore, EG also has a positive effect on the oligomerization during the crystal growth process, leading to the formation of high crystalline nanosheets. The surface of obtained nanosheets is very smooth, which can be ascribed to Ostwald ripening. $Zn_3V_2O_7(OH)_2{\cdot}2H_2O$ counterparts prepared with different amounts (80 mL named ZnVO-80, 160 mL named ZnVO-1, 240 mL named ZnVO-240) of EG were also compared. From the XRD patterns (Figure S4) and SEM images (Figure S5), it is found that, compared with ZnVO-80, ZnVO-1 and ZnVO-240 display higher crystallinity and a more regular and uniform morphology, which could be attributed to the oligomerization effect of EG during the synthesis process. However, the introduction of EG could reduce the reaction rate and control the crystal growth. The more EG is introduced into the reaction, the longer reaction time is needed to obtain a certain yield. Therefore, the addition of 160 mL of EG is sufficient and cost-effective to obtain highly crystallized $Zn_3V_2O_7(OH)_2{\cdot}2H_2O$ nanosheet-assembled microflowers.

The cycling performance of ZnVO-1 and ZnVO-2 at the current density of 500 mA g^{-1} is compared to confirm the structure superiority of ZnVO-1 (Figure S6). The ZnVO-1 delivers high initial discharge/charge capacities of 1397 and 697 mA h g^{-1}, respectively. It is interesting that the discharge capacity increases gradually after the initial decrease, which stabilizes at 891 mA h g^{-1} after 140 cycles. The initial discharge/charge capacities of ZnVO-2 are 1383 and 687 mA h g^{-1}, respectively, showing no great difference from that of ZnVO-1. However, the discharge capacity fades rapidly in the following electrochemical process and a lower capacity of 553 mA h g^{-1} is remained at the end of 140 cycles. The initial

DOI: 10.1021/acsami.7b06996
ACS Appl. Mater. Interfaces 2017, 9, 27707−27714

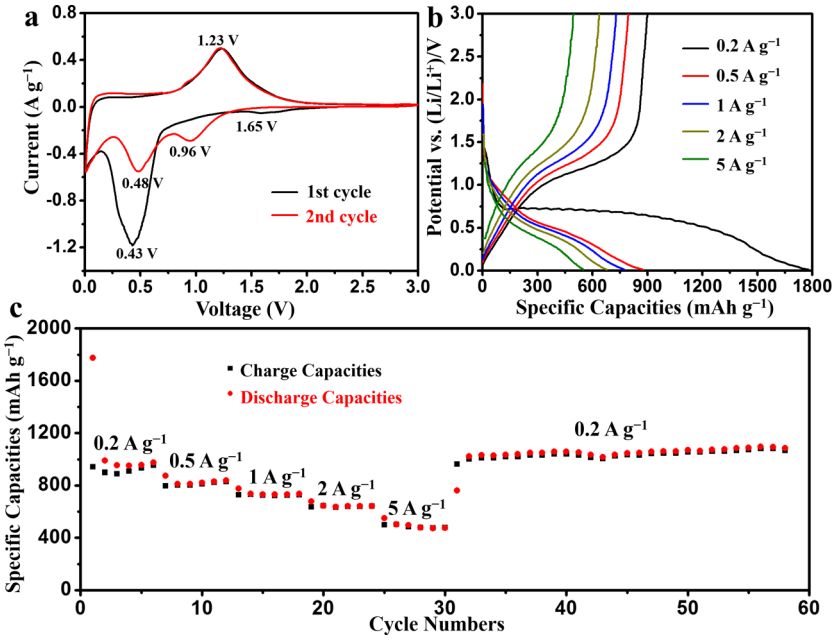

Figure 3. (a) CV curves of the first two cycles of the ZnVO-1 electrode at a scan rate of 0.1 mV s^{-1}. (b) Galvanostatic charge/discharge profiles at different current densities during rate performance test. (c) The rate performance of ZnVO-1 electrode at different current densities.

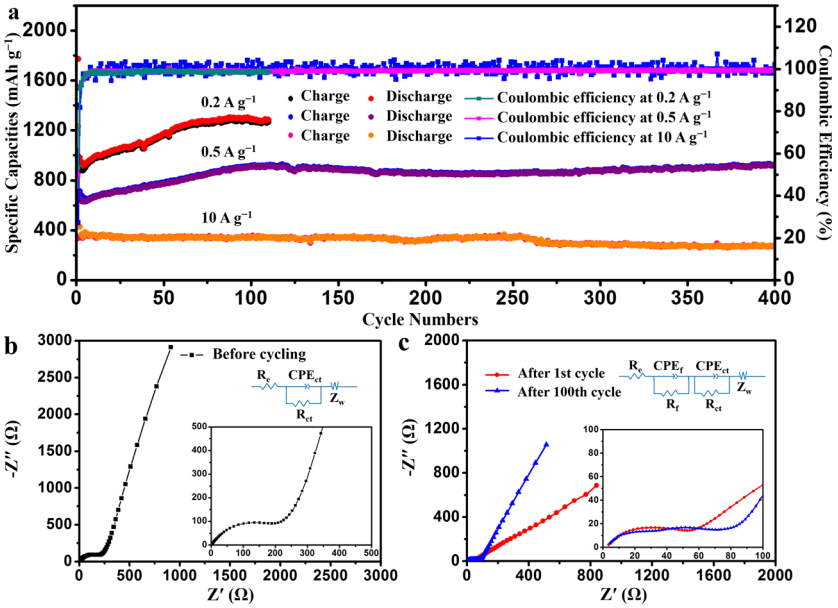

Figure 4. (a) Cycling performance and corresponding Coulombic efficiency of ZnVO-1 at 0.2, 0.5, and 10 A g^{-1}. (b, c) The typical Nyquist plots of ZnVO-1 before cycling and at different cycles. The insets are the equivalent circuits.

electrochemical performance comparison is in accordance with the structure characterizations, as ZnVO-1 and ZnVO-2 have a similar ultrathin nanosheet-assembled microflowers structure. However, the higher-crystalline structure of ZnVO-1 can act as a stable host for the ion diffusion/electron conduction process, leading to the excellent cycling stability.

The cyclic voltammetry (CV) test of the ZnVO-1 electrode was carried out at a scan rate of 0.1 mV s^{-1} in the potential window of 0.01−3.0 V (Figure 3a). The peak at 1.65 V during the first discharge process indicates that the Li^+ inserts into $Zn_3V_2O_7(OH)_2{\cdot}2H_2O$ without phase decomposition, which is then confirmed by the ex situ XRD result in the following discussion. The cathodic peak at 0.43 V could be assigned to the decomposition of $Li_xZn_3V_2O_7(OH)_2{\cdot}2H_2O$ into zinc oxide and lithium vanadium oxide, the reduction of ZnO to Zn, and the reduction process of lithium vanadium oxide, accompanied by the formation of a solid electrolyte interface (SEI). The further alloying process of Li-Zn corresponds to the lower cathodic peak. The broad anodic peak at 1.23 V can be assigned to the formation of ZnO from the Li-Zn alloy and reversible extraction of lithium ions from lithium vanadium oxide. Due to the irreversible structure change of $Zn_3V_2O_7(OH)_2{\cdot}2H_2O$ in the first discharge process, the subsequent CV curves are different from the initial one. Two shifted cathodic peaks at 0.96 and 0.48 V and one unchanged anodic peak at 1.23 V can

DOI: 10.1021/acsami.7b06996
ACS Appl. Mater. Interfaces 2017, 9, 27707−27714

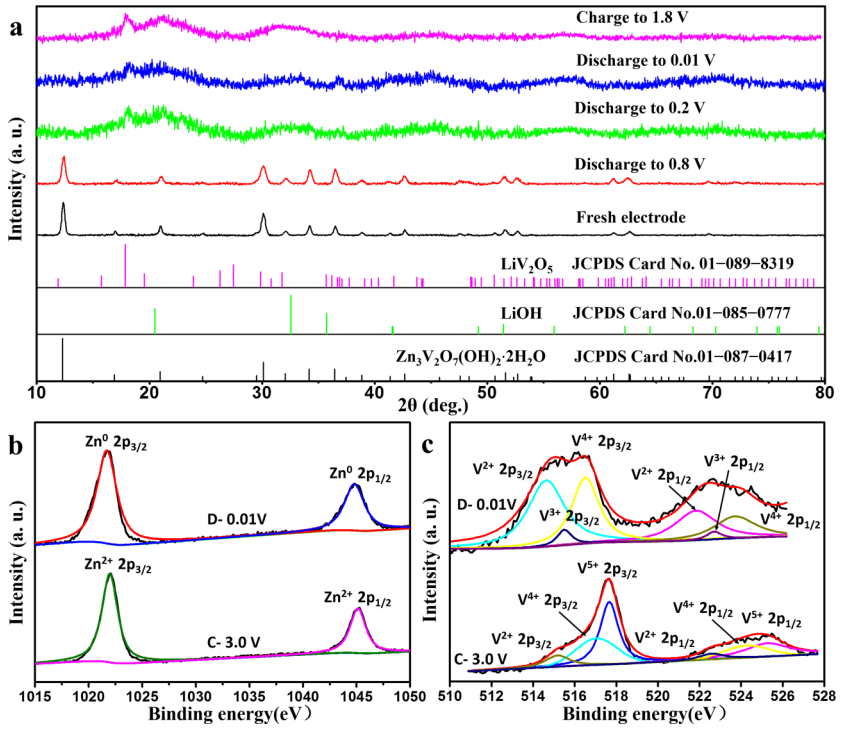

Figure 5. (a) Ex situ XRD patterns of ZnVO-1 electrode at different voltages in the first cycle. (b) High-resolution Zn 2p XPS spectrum. (c) High-resolution V 2p XPS spectrum of lithiated ZnVO-1 electrode (discharged to 0.01 V) and delithiated ZnVO-1 electrode (charged to 3.0 V).

be observed, indicating the irreversible electrochemical reaction in the first discharge process.[14]

To investigate the rate capability of ZnVO-1, the sample was cycled under the increasing current densities from 0.2 to 5.0 A g^{-1} (Figure 3c). The ZnVO-1 anode exhibits an excellent cycling response under different current densities. Attractively, the ZnVO-1 exhibits decent second cycle discharge capacities of 991, 812, 736, 645, and 501 mA h g^{-1} at current densities of 0.2, 0.5, 1.0, 2.0, and 5.0 A g^{-1}, respectively. Particularly, even when the current increases to 25 times of the original current, the discharge specific capacity maintains 51% of the original value. More significantly, a high discharge capacity of 1024 mA h g^{-1} is recovered when the current density reduces back to 0.2 A g^{-1}, even higher than that of the original value, confirming the high structural stability of the ZnVO-1.

Figure 4a demonstrates the cycling performance of ZnVO-1 anode at current densities of 0.2, 0.5, and 10 A g^{-1} in the potential range of 0.01−3.0 V (vs Li/Li^+). A high reversible specific discharge capacity of 983 mA h g^{-1} is delivered at the second cycle at the current density of 0.2 A g^{-1}, which gradually increases to 1287 mA h g^{-1} after 120 cycles. The initial Coulombic efficiency is 53%, and the capacity loss during the initial few cycles can be ascribed to the irreversible decomposition of electrolyte and crystal reconstruction of the ZnVO-1. The following capacity increase could be ascribed to the activation process, reversible reaction between LiOH and Li_2O, and repetitive formation of a polymeric gel-like film resulting from kinetically activated electrolyte degradation, which is a common phenomenon among metal oxides according to previous studies.[50,51] Under the current density of 0.5 A g^{-1}, the ZnVO-1 electrode delivers a reversible discharge capacity of 711 mA h g^{-1}. The discharge capacity gradually increases during the subsequent 100 cycles and retains a value as high as 931 mA h g^{-1} after 400 cycles. It is worth noting that a high reversible discharge capacity of 428 mA h g^{-1} can be obtained at the high current density of 10 A g^{-1} and maintains as 272 mA h g^{-1} after 400 cycles, which can be ascribed to the fast reaction kinetics of the $Zn_3V_2O_7(OH)_2\cdot 2H_2O$ electrode. More impressively, the ZnVO-1 electrode can retain a discharge capacity of 298 mA h g^{-1} at the high current density of 5 A g^{-1} after 1400 cycles (Figure S7), corresponding to the capacity retention of 51% from the 2nd to 1400th cycle (an average loss of only 0.048% per cycle). The superior rate capability and cycling performance of ZnVO-1 could be ascribed to the fast electron transport in ultrathin nanosheets and the facile lithium-ion diffusion due to the voids between electrode and electrolyte. In addition, we compared the electrode performance of ZnVO-1 with other zinc vanadium oxides anode materials in Table S1. To our knowledge, this is the best electrochemical performance for $Zn_3V_2O_7(OH)_2\cdot 2H_2O$ anode material and one of the best zinc vanadium oxide electrodes ever reported.

To further elucidate the superior electrochemical performance of the ZnVO-1 electrode, the electrochemical impedance spectrum (EIS) evaluations before and after different cycles were conducted (Figure 4b,c). According to the previous literatures, the high frequency region is related to the solid electrolyte interphase (SEI) resistance, and the middle frequency region reveals the charge transfer resistance, while the low frequency region reflects the Li-ion diffusion characteristic in the active material.[52] Different equivalence circuits are applied to fit the AC impedance spectra before and after cycling (inset of Figure 4b,c), as one semicircle has evolved into two semicircles at high and middle frequencies with the increasing cycles, which could be attributed to the formation of the SEI layer on the surface of the active material. Quantitative analysis was carried out according to the equivalence circuits. The charge transfer resistance (R_{ct}) reduces from 223 to 35 Ω after the first cycle. Then the increase of R_{ct} from 35 to 71 Ω can be attributed the formation of the solid electrolyte interface film

DOI: 10.1021/acsami.7b06996
ACS Appl. Mater. Interfaces 2017, 9, 27707−27714

after 100 cycles. Meanwhile, compared with the first cycle, the slope at low frequency after 100 cycles increases, reflecting the lithium-ion transport efficiency is enhanced with increase of cycling process. The decreased charge transfer resistance and increased lithium-ion transport efficiency are beneficial for the fast ion/electron transport and reaction during the charge/discharge process, thus improving the reaction kinetics of the active materials.

The ex situ SEM and TEM images after 100 cycles are displayed in Figure S8 to characterize the morphological change after the electrochemical process. It is interesting that the ultrathin nanosheets have changed into closely packed nanoparticles assembled nanosheets. The uniformly distributed nanoparticles can provide a favorable reduced lithium-ion diffusion pathway, which is beneficial for the rate capability. This structure transition can be ascribed to the autogenous nanocrystallization process, which can effectively prevent the structure pulverization during the electrochemical process, leading to a high mechanical flexibility to accommodate the volume expansion during cycling,[53] resulting in excellent cycling performance.

Ex situ XRD in Figure 5a was performed at different states during the first charging/discharging process. When the ZnVO-1 anode material was discharged to 0.8 V, the peaks position of the electrode has no change. However, the peak intensity has decreased slightly. On the basis of this result, we can conclude that the lithium-ions insertion at 1.65 V does not cause the phase transformation of $Zn_3V_2O_7(OH)_2{\cdot}2H_2O$ crystals. When further discharged to 0.2 V, the peaks of electrode are indexed to the combination of $Li_{1+x}V_2O_5$ and LiOH. The generation of LiOH should be the reaction product of Li_2O and crystal water in the structure. The decomposition of the electrolyte combining with the existence of crystal water lead to the formation of LiOH. The conversion reaction of LiOH + $2Li^+$ + $2e^-$ ↔ Li_2O + LiH could provide an additional capacity of $Zn_3V_2O_7(OH)_2{\cdot}2H_2O$ system.[54,55] It is interesting that there are no other products detected from the XRD pattern, which could be attributed to the amorphous state of the final reaction product. The XRD patterns of the electrode discharged to 0.01 V and charged to 1.8 V are similar. However, the peaks intensity of $Li_{1+x}V_2O_5$ has been enhanced when the cell was charged to 1.8 V, indicating the ever-increasing crystallinity of $Li_{1+x}V_2O_5$ during the charging process. The following cycling process mainly includes lithiation/delithiation of $Li_{1+x}V_2O_5$, the conversion reaction of ZnO, combining with the alloying reaction of Zn. The ex situ XRD patterns in the 30th cycles are displayed in Figure S9. The variation of the peak intensity of $Li_{1+x}V_2O_5$ during the charge and discharge process reveals that the insertion reaction of lithium vanadium oxide is reversible. In addition, the reaction between LiOH and Li_2O is invertible during the electrochemical reaction, which is confirmed by the XRD peak density variation of LiOH during the electrochemical process of the 30th cycles.

Ex situ X-ray photoelectron spectroscopy (XPS) characterization was performed at different voltages during the initial discharging/charging process. In Figure S10, the X-ray photoelectron spectroscopy of the fresh ZnVO-1 electrode reveals high-resolution Zn 2p and V 2p spectra. The binding energy V $2p_{3/2}$ peak at 517.3 eV and Zn $2p_{3/2}$ peak at 1022.1 eV can be ascribed to the V^{5+} and Zn^{2+}. When the electrode was discharged to 0.01 V, the binding energy of 1021.6 and 1044.7 eV (Figure 5b) can be ascribed to metallic Zn $2p_{3/2}$ and Zn $2p_{1/2}$, which indicates the formation of Li-Zn alloy after the initial discharging. After charged to 3.0 V, the peak binding energy of the element Zn 2p spectrum increased to 1022 and 1045.1 eV, which reflects the oxidation of Zn^0 to Zn^{2+}. When discharged to 0.01 V, the high-resolution V $2p_{3/2}$ XPS spectrum in Figure 5c can be deconvoluted into V^{4+} (516.5 eV), V^{3+} (515.5 eV), and V^{2+} (514.7 eV), and the corresponding binding energies for V $2p_{1/2}$ of V^{4+}, V^{3+}, and V^{2+} are 523.7, 522.7, and 521.8 eV separately. When charging to 3.0 V, most vanadium elements were oxidized to V^{4+} and V^{5+}, corresponding to the binding energy of V $2p_{3/2}$ (515.6 eV, 517.1 eV) and V $2p_{1/2}$ (522.8 eV, 524.3 eV). In addition, the binding energy peaks at 514.7 and 521.9 eV in the V 2p spectrum could be indexed to residual V^{2+} obtained after the discharging process, indicating the existence of a small amount of irreversible vanadium oxide during the electrochemical process. From the ex situ XPS and ex situ XRD results, the alloying and conversion reaction between Li-Zn and ZnO, accompanying with the intercalation reaction of lithium vanadium oxides, contribute to the high capacity of the $Zn_3V_2O_7(OH)_2{\cdot}2H_2O$ electrode.

4. CONCLUSION

In summary, the high crystalline $Zn_3V_2O_7(OH)_2{\cdot}2H_2O$ nanosheet-assembled microflowers are synthesized via a simple liquid phase method at room temperature. The synthetic method can be easily applied for the large-scale synthesis in industry. The EG can restrict the growth of crystal nuclei and enhance the crystallinity of the product effectively. The highly crystallized $Zn_3V_2O_7(OH)_2{\cdot}2H_2O$ nanosheet-assembled microflowers deliver excellent electrochemical performance with stable cycling performance and high rate capability. The nanosheet-assembled $Zn_3V_2O_7(OH)_2{\cdot}2H_2O$ microflowers show a high discharge capacity (1287 mA h g^{-1} at 0.2 A g^{-1} after 120 cycles), excellent rate performance (501 mA h g^{-1} at 5 A g^{-1}), and long cycling stability (298 mA h g^{-1} at 5 A g^{-1} after 1400 cycles). This could be attributed to the unique nanosheet-assembled microflowers structure, which can provide facile and fast ion/electron pathway for the ZnVO-1 electrode during cycling. Combining with the easily scaled up method, the as-prepared $Zn_3V_2O_7(OH)_2{\cdot}2H_2O$ can be a highly promising anode for commercial LIBs.

■ ASSOCIATED CONTENT

Supporting Information

The Supporting Information is available free of charge on the ACS Publications website at DOI: 10.1021/acsami.7b06996.

The morphology and electrochemical performance of the products were investigated by SEM, TEM, BET, and battery testing system (PDF)

■ AUTHOR INFORMATION

Corresponding Authors

*E-mail: mlq518@whut.edu.cn (L.M.).

*E-mail: luoyanzhu@mail.hzau.edu.cn (Y.L.).

ORCID

Liqiang Mai: 0000-0003-4259-7725

Author Contributions

The manuscript was written through contributions of all authors. All authors have given approval to the final version of the manuscript.

Notes

The authors declare no competing financial interest.

DOI: 10.1021/acsami.7b06996
ACS Appl. Mater. Interfaces 2017, 9, 27707−27714

■ ACKNOWLEDGMENTS

This work was supported by the National Key Research and Development Program of China (2016YFA0202603, 2016YFA0202604), the National Basic Research Program of China (2013CB934103), the Programme of Introducing Talents of Discipline to Universities (B17034), the National Natural Science Foundation of China (51521001, 51502227, 51579198), the National Natural Science Fund for Distinguished Young Scholars (51425204), the China Postdoctoral Science Foundation (2015T80845), the Hubei Province Natural Science Fund (2016CFB582), and the Fundamental Research Funds for the Central Universities (WUT: 2016III001, 2016III005, 2017III009, 2017III005, 2017III030). Prof. Liang He and Prof. Liqiang Mai gratefully acknowledge the financial support from the China Scholarship Council (Nos. 201606955094, 201606955096).

■ REFERENCES

(1) Armand, M.; Tarascon, J. M. Building Better Batteries. *Nature* **2008**, *451*, 652−657.
(2) Magasinski, A.; Dixon, P.; Hertzberg, B.; Kvit, A.; Ayala, J.; Yushin, G. High-Performance Lithium-Ion Anodes Using a Hierarchical Bottom-up Approach. *Nat. Mater.* **2010**, *9*, 353−358.
(3) Yuan, C.; Wu, H. B.; Xie, Y.; Lou, X. W. Mixed Transition-Metal Oxides: Design, Synthesis, and Energy-Related Applications. *Angew. Chem., Int. Ed.* **2014**, *53*, 1488−1504.
(4) Liang, H.; Ni, J.; Li, L. Bio-Inspired Engineering of Bi_2S_3-PPy Yolk-Shell Composite for Highly Durable Lithium and Sodium Storage. *Nano Energy* **2017**, *33*, 213−220.
(5) Bai, J.; Li, X.; Liu, G.; Qian, Y.; Xiong, S. Unusual Formation of $ZnCo_2O_4$ 3D Hierarchical Twin Microspheres as a High-Rate and Ultralong-Life Lithium-Ion Battery Anode Material. *Adv. Funct. Mater.* **2014**, *24*, 3012−3020.
(6) An, Q.; Lv, F.; Liu, Q.; Han, C.; Zhao, K.; Sheng, J.; Wei, Q.; Yan, M.; Mai, L. Amorphous Vanadium Oxide Matrixes Supporting Hierarchical Porous Fe_3O_4/Graphene Nanowires as a High-Rate Lithium Storage Anode. *Nano Lett.* **2014**, *14*, 6250−6256.
(7) Hou, L.; Lian, L.; Zhang, L.; Pang, G.; Yuan, C.; Zhang, X. Self-Sacrifice Template Fabrication of Hierarchical Mesoporous Bi-Component-Active ZnO/$ZnFe_2O_4$ Sub-Microcubes as Superior Anode Towards High-Performance Lithium-Ion Battery. *Adv. Funct. Mater.* **2015**, *25*, 238−246.
(8) Chen, Z.; Zhou, M.; Cao, Y.; Ai, X.; Yang, H.; Liu, J. In Situ Generation of Few-Layer Graphene Coatings on SnO_2-SiC Core-Shell Nanoparticles for High-Performance Lithium-Ion Storage. *Adv. Energy Mater.* **2012**, *2*, 95−102.
(9) Raju, V.; Wang, X.; Luo, W.; Ji, X. Multiple Ambient Hydrolysis Deposition of Tin Oxide into Nanoporous Carbon to Give a Stable Anode for Lithium-Ion Batteries. *Chem. - Eur. J.* **2014**, *20*, 7686−7691.
(10) Liu, B.; Zhang, J.; Wang, X. F.; Chen, G.; Chen, D.; Zhou, C. W.; Shen, G. Z. Hierarchical Three-Dimensional $ZnCo_2O_4$ Nanowire Arrays/Carbon Cloth Anodes for a Novel Class of High-Performance Flexible Lithium-Ion Batteries. *Nano Lett.* **2012**, *12*, 3005−3011.
(11) Yu, L.; Zhang, L.; Wu, H. B.; Zhang, G.; Lou, X. W. Controlled Synthesis of Hierarchical $Co_xMn_{3-x}O_4$ Array Micro-/Nanostructures with Tunable Morphology and Composition as Integrated Electrodes for Lithium-Ion Batteries. *Energy Environ. Sci.* **2013**, *6*, 2664−2671.
(12) Zhu, J.; Xu, Z.; Lu, B. Ultrafine Au Nanoparticles Decorated $NiCo_2O_4$ Nanotubes as Anode Material for High-Performance Supercapacitor and Lithium-Ion Battery Applications. *Nano Energy* **2014**, *7*, 114−123.
(13) Denis, S.; Baudrin, E.; Orsini, F.; Ouvrard, G.; Touboul, M.; Tarascon, J. M. Synthesis and Electrochemical Properties of Numerous Classes of Vanadates. *J. Power Sources* **1999**, *81*−*82*, 79−84.
(14) Yin, Z.; Qin, J.; Wang, W.; Cao, M. Rationally Designed Hollow Precursor-Derived $Zn_3V_2O_8$ Nanocages as a High-Performance Anode Material for Lithium-Ion Batteries. *Nano Energy* **2017**, *31*, 367−376.
(15) Wu, F.; Yu, C.; Liu, W.; Wang, T.; Feng, J.; Xiong, S. Large-Scale Synthesis of $Co_2V_2O_7$ Hexagonal Microplatelets under Ambient Conditions for Highly Reversible Lithium Storage. *J. Mater. Chem. A* **2015**, *3*, 16728−16736.
(16) Luo, Y.; Xu, X.; Zhang, Y.; Chen, C.; Zhou, L.; Yan, M.; Wei, Q.; Tian, X.; Mai, L. Graphene Oxide Templated Growth and Superior Lithium Storage Performance of Novel Hierarchical $Co_2V_2O_7$ Nanosheets. *ACS Appl. Mater. Interfaces* **2016**, *8*, 2812−2818.
(17) Yang, G.; Cui, H.; Yang, G.; Wang, C. Self-Assembly of $Co_3V_2O_8$ Multi Layered Nanosheets: Controllable Synthesis, Excellent Li-Storage Properties, and Investigation of Electrochemical Mechanism. *ACS Nano* **2014**, *8*, 4474−4487.
(18) Wu, F.; Xiong, S.; Qian, Y.; Yu, S. Hydrothermal Synthesis of Unique Hollow Hexagonal Prismatic Pencils of $Co_3V_2O_8{\cdot}nH_2O$: A New Anode Material for Lithium-Ion Batteries. *Angew. Chem., Int. Ed.* **2015**, *54*, 10787−10791.
(19) Soundharrajan, V.; Sambandam, B.; Song, J.; Kim, S.; Jo, J.; Kim, S.; Lee, S.; Mathew, V.; Kim, J. $Co_3V_2O_8$ Sponge Network Morphology Derived from Metal−Organic Framework as an Excellent Lithium Storage Anode Material. *ACS Appl. Mater. Interfaces* **2016**, *8*, 8546−8553.
(20) Sim, D. H.; Rui, X.; Chen, J.; Tan, H.; Lim, T. M.; Yazami, R.; Hng, H. H.; Yan, Q. Direct Growth of $FeVO_4$ Nanosheet Arrays on Stainless Steel Foil as High-Performance Binder-Free Li Ion Battery Anode. *RSC Adv.* **2012**, *2*, 3630−3633.
(21) Liu, X.; Cao, Y.; Zheng, H.; Chen, X.; Feng, C. Synthesis and Modification of $FeVO_4$ as Novel Anode for Lithium-Ion Batteries. *Appl. Surf. Sci.* **2017**, *394*, 183−189.
(22) Gan, L.; Deng, D.; Zhang, Y.; Li, G.; Wang, X.; Jiang, L.; Wang, C. $Zn_3V_2O_8$ Hexagon Nanosheets: A High-Performance Anode Material for Lithium-Ion Batteries. *J. Mater. Chem. A* **2014**, *2*, 2461−2466.
(23) Yang, G.; Wu, M.; Wang, C. Ultrathin $Zn_2(OH)_3VO_3$ Nanosheets: First Synthesis, Excellent Lithium-Storage Properties, and Investigation of Electrochemical Mechanism. *ACS Appl. Mater. Interfaces* **2016**, *8*, 23746−23754.
(24) Yin, L.; Zhang, Z.; Li, Z.; Hao, F.; Li, Q.; Wang, C.; Fan, R.; Qi, Y. Spinel $ZnMn_2O_4$ Nanocrystal-Anchored 3D Hierarchical Carbon Aerogel Hybrids as Anode Materials for Lithium Ion Batteries. *Adv. Funct. Mater.* **2014**, *24*, 4176−4185.
(25) Zheng, C.; Zeng, L.; Wang, M.; Zheng, H.; Wei, M. Synthesis of Hierarchical ZnV_2O_4 Microspheres and Its Electrochemical Properties. *CrystEngComm* **2014**, *16*, 10309−10313.
(26) Bie, C.; Pei, J.; Chen, G.; Zhang, Q.; Sun, J.; Yu, Y.; Chen, D. Hierarchical $Zn_3V_3O_8$/C Composite Microspheres Assembled from Unique Porous Hollow Nanoplates with Superior Lithium Storage Capability. *J. Mater. Chem. A* **2016**, *4*, 17063−17072.
(27) Yu, Y.; Niu, C.; Han, C.; Zhao, K.; Meng, J.; Xu, X.; Zhang, P.; Wang, L.; Wu, Y.; Mai, L. Zinc Pyrovanadate Nanoplates Embedded in Graphene Networks with Enhanced Electrochemical Performance. *Ind. Eng. Chem. Res.* **2016**, *55*, 2992−2999.
(28) Chen, R.; Hu, Y.; Shen, Z.; Chen, Y.; He, X.; Zhang, X.; Zhang, Y. Controlled Synthesis of Carbon Nanofibers Anchored with $Zn_xCo_{3-x}O_4$ Nanocubes as Binder-Free Anode Materials for Lithium-Ion Batteries. *ACS Appl. Mater. Interfaces* **2016**, *8*, 2591−2599.
(29) Vijayakumar, S.; Lee, S. H.; Ryu, K. S. Synthesis of $Zn_3V_2O_8$ Nanoplatelets for Lithium-Ion Battery and Supercapacitor Applications. *RSC Adv.* **2015**, *5*, 91822−91828.
(30) Sun, Y.; Li, C.; Wang, L.; Wang, Y.; Ma, X.; Ma, P.; Song, M. Ultralong Monoclinic ZnV_2O_6 Nanowires: Their Shape-Controlled Synthesis, New Growth Mechanism, and Highly Reversible Lithium Storage in Lithium-Ion Batteries. *RSC Adv.* **2012**, *2*, 8110−8115.
(31) Zhang, S.; Lei, N.; Ma, W.; Zhang, Z.; Sun, Z.; Wang, Y. Fabrication of Ultralong $Zn_3V_2O_7(OH)_2{\cdot}2H_2O$ Nanobelts and Its Application in Lithium-Ion Batteries. *Mater. Lett.* **2014**, *129*, 91−94.
(32) Ryu, J.; Hong, D.; Choi, S.; Park, S. Synthesis of Ultrathin Si Nanosheets from Natural Clays for Lithium-Ion Battery Anodes. *ACS Nano* **2016**, *10*, 2843−2851.

DOI: 10.1021/acsami.7b06996
ACS Appl. Mater. Interfaces 2017, 9, 27707−27714

(33) Mahmood, N.; Tang, T.; Hou, Y. Nanostructured Anode Materials for Lithium Ion Batteries: Progress, Challenge and Perspective. *Adv. Energy Mater.* **2016**, *6*, 1600374.
(34) Jiang, B.; Zeng, S.; Wang, H.; Liu, D.; Qian, J.; Cao, Y.; Yang, H.; Ai, X. Dual Core-Shell Structured Si@SiO_x@C Nanocomposite Synthesized via a One-Step Pyrolysis Method as a Highly Stable Anode Material for Lithium-Ion Batteries. *ACS Appl. Mater. Interfaces* **2016**, *8*, 31611−31616.
(35) Lv, C.; Sun, J.; Chen, G.; Yan, C.; Chen, D. Achieving $Ni_3V_2O_8$ Amorphous Wire Encapsulated in Crystalline Tube Nanostructure as Anode Materials for Lithium Ion Batteries. *Nano Energy* **2017**, *33*, 138−145.
(36) Geim, A. K.; Novoselov, K. S. The Rise of Graphene. *Nat. Mater.* **2007**, *6*, 183−191.
(37) Takada, K.; Sakurai, H.; Takayama Muromachi, E.; Izumi, F.; Dilanian, R. A.; Sasaki, T. Superconductivity in Two-Dimensional CoO_2 Layers. *Nature* **2003**, *422*, 53−55.
(38) Hitz, E.; Wan, J.; Patel, A.; Xu, Y.; Meshi, L.; Dai, J.; Chen, Y.; Lu, A.; Davydov, A. V.; Hu, L. Electrochemical Intercalation of Lithium Ions into $NbSe_2$ Nanosheets. *ACS Appl. Mater. Interfaces* **2016**, *8*, 11390−11395.
(39) Niu, C.; Huang, M.; Wang, P.; Meng, J.; Liu, X.; Wang, X.; Zhao, K.; Yu, Y.; Wu, Y.; Lin, C.; Mai, L. Carbon-Supported and Nanosheet-Assembled Vanadium Oxide Microspheres for Stable Lithium-Ion Battery Anodes. *Nano Res.* **2016**, *9*, 128−138.
(40) Shi, Y.; Huang, J. K.; Jin, L.; Hsu, Y. T.; Yu, S. F.; Li, L. J.; Yang, H. Y. Selective Decoration of Au Nanoparticles on Monolayer MoS_2 Single Crystals. *Sci. Rep.* **2013**, *3*, 1839.
(41) Sreeprasad, T. S.; Nguyen, P.; Kim, N.; Berry, V. Controlled, Defect-Guided, Metal-Nanoparticle Incorporation onto MoS_2 via Chemical and Microwave Routes: Electrical, Thermal, and Structural Properties. *Nano Lett.* **2013**, *13*, 4434−4441.
(42) Su, K.; Wang, C.; Nie, H.; Guan, Y.; Liu, F.; Chen, J. Facile Template-Free Synthesis of 3D Porous MnO/C Microspheres with Controllable Pore Size for High-Performance Lithium-Ion Battery Anodes. *J. Mater. Chem. A* **2014**, *2*, 10000−10006.
(43) Chirayil, T.; Zavalij, P. Y.; Whittingham, M. S. Hydrothermal Synthesis of Vanadium Oxides. *Chem. Mater.* **1998**, *10*, 2629−2640.
(44) Nam, K. W.; Kim, S.; Lee, S.; Salama, M.; Shterenberg, I.; Gofer, Y.; Kim, J. S.; Yang, E.; Park, C. S.; Kim, J. S.; Lee, S. S.; Chang, W. S.; Doo, S. G.; Jo, Y. N.; Jung, Y.; Aurbach, D.; Choi, J. W. The High Performance of Crystal Water Containing Manganese Birnessite Cathodes for Magnesium Batteries. *Nano Lett.* **2015**, *15*, 4071−4079.
(45) Le, Z.; Liu, F.; Nie, P.; Li, X.; Liu, X.; Bian, Z.; Chen, G.; Wu, H. B.; Lu, Y. Pseudocapacitive Sodium Storage in Mesoporous Single-Crystal-Like TiO_2-Graphene Nanocomposite Enables High-Performance Sodium-Ion Capacitors. *ACS Nano* **2017**, *11*, 2952.
(46) Lü, Y.; Zhan, W.; He, Y.; Wang, Y.; Kong, X.; Kuang, Q.; Xie, Z.; Zheng, L. MOF-Templated Synthesis of Porous Co_3O_4 Concave Nanocubes with High Specific Surface Area and Their Gas Sensing Properties. *ACS Appl. Mater. Interfaces* **2014**, *6*, 4186−4195.
(47) Zhong, L.; Hu, J.; Liang, H.; Cao, A.; Song, W.; Wan, L. Self-Assembled 3D Flowerlike Iron Oxide Nanostructures and Their Application in Water Treatment. *Adv. Mater.* **2006**, *18*, 2426−2431.
(48) Zhang, S.; Xiao, X.; Lu, M.; Li, Z. $Zn_3V_2O_7(OH)_2{\cdot}2H_2O$ and $Zn_3(VO_4)_2$ 3D Microspheres as Anode Materials for Lithium-Ion Batteries. *J. Mater. Sci.* **2013**, *48*, 3679−3685.
(49) Jiang, X.; Wang, Y.; Herricks, T.; Xia, Y. Ethylene Glycol-Mediated Synthesis of Metal Oxide Nanowires. *J. Mater. Chem.* **2004**, *14*, 695−703.
(50) Zheng, F.; Zhu, D.; Chen, Q. Facile Fabrication of Porous $Ni_xCo_{3-x}O_4$ Nanosheets with Enhanced Electrochemical Performance as Anode Materials for Li-Ion Batteries. *ACS Appl. Mater. Interfaces* **2014**, *6*, 9256−9264.
(51) Huang, S.; Zhang, L.; Lu, X.; Liu, L.; Liu, L.; Sun, X.; Yin, Y.; Oswald, S.; Zou, Z.; Ding, F.; Schmidt, O. G. Tunable Pseudocapacitance in 3D $Tio_{2-\delta}$ Nanomembranes Enabling Superior Lithium Storage Performance. *ACS Nano* **2017**, *11*, 821−830.
(52) Huang, X.; Cui, S.; Chang, J.; Hallac, P. B.; Fell, C. R.; Luo, Y.; Metz, B.; Jiang, J.; Hurley, P. T.; Chen, J. A Hierarchical Tin/Carbon Composite as an Anode for Lithium-Ion Batteries with a Long Cycle Life. *Angew. Chem.* **2015**, *127*, 1510−1513.
(53) Wang, X.; Chen, D.; Yang, Z.; Zhang, X.; Wang, C.; Chen, J.; Zhang, X.; Xue, M. Novel Metal Chalcogenide SnSSe as a High-Capacity Anode for Sodium-Ion Batteries. *Adv. Mater.* **2016**, *28*, 8645−8650.
(54) Yu, W.; Zhang, L.; Hou, P.; Li, F.; Liu, C.; Cheng, H. High Reversible Lithium Storage Capacity and Structural Changes of Fe_2O_3 Nanoparticles Confined inside Carbon Nanotubes. *Adv. Energy Mater.* **2016**, *6*, 1501755.
(55) Hu, Y.; Liu, Z.; Nam, K. W.; Borkiewicz, O. J.; Cheng, J.; Hua, X.; Dunstan, M. T.; Yu, X.; Wiaderek, K. M.; Du, L. S.; Chapman, K. W.; Chupas, P. J.; Yang, X.; Grey, C. P. Origin of Additional Capacities in Metal Oxide Lithium-Ion Battery Electrodes. *Nat. Mater.* **2013**, *12*, 1130−1136.

NOTE ADDED AFTER ASAP PUBLICATION

This paper was published on the Web on August 8, 2017, with a minor text error on page five of the document. The corrected version was reposted on August 9, 2017.

DOI: 10.1021/acsami.7b06996
ACS Appl. Mater. Interfaces 2017, 9, 27707−27714